Eur. Phys. J. Plus (2019) **134**: 34
DOI 10.1140/epjp/i2019-12432-6

THE EUROPEAN PHYSICAL JOURNAL PLUS

Regular Article

A novel algorithm for the detection of cerebral aneurysm using sub-band morphological operation

Hira Khan[1], Muhammad Sharif[1], Nargis Bibi[2], and Nazeer Muhammad[1,a]

[1] COMSATS University Islamabad, Wah Campus, Islamabad, Pakistan
[2] Fatima Jinnah Women University, Rawalpindi, Pakistan

Received: 13 May 2018 / Revised: 13 October 2018
Published online: 22 January 2019

Abstract. Junctions or portions of blood vessels may sometimes develop weak spots because of certain factors like high blood pressure, head trauma, and infection. With time, these weak spots result in bulging or ballooning out or filling with blood creating some sac-like structures known as aneurysm. These structures can burst by leaking blood into the nearby tissues as a result of artery spam known as the subarachnoid hemorrhage, which leads to potential stroke and even death. In this regard, patients' outcome is treated before the ruptured detection during the setting up of the aneurysm process. It is considered as a much better approach than the treatment after the aneurysm process. Neurosurgeons prefer two treatment options that are clipping and coiling, which demand sufficient detection of cerebral aneurysm. To facilitate expert neurosurgeons, we propose a novel method to determine an automatic cerebral aneurysm in the domain of digital subtraction angiography. It is processed by using the sub-band morphological operation in the wavelet domain. Simulation results have demonstrated the proposed method in order to prove efficiency in terms of accurate detection with impartial location, definite size, and firm type of aneurysm.

1 Introduction

Due to infection, trauma, and high blood pressure the walls of blood vessels may weaken, causing abnormal swelling called an aneurysm [1]. With the increase in blood pressure, weak spots of blood vessels balloon are exploding. The occurrence of this aneurysm in brain vessels is termed as cerebral aneurysm (CA). This is a kind of neurological disorder of cerebral arteries [2]. CAs can be unevenly classified into terminal, lateral, and bifurcation aneurysms. Their classification depends upon their relation to their parent artery [3]. The wall of blood vessels weakens the net results in ballooning out of the vessel that fills with blood. These swallowed portions of blood vessels in brain can rupture and this risk varies with size, location, and type depending upon the condition of the aneurysms. This rupture results in blood leakage around vessels causing life threatening subarachnoid hemorrhage (SAH). About 3% of the population has more than one cerebral aneurysms [4]. The relative distribution of patients upon admission according to the method of [5] is shown in tables.

The death rate due to pathological occurrences is recorded to be almost 50%, while the remaining 46% of survivors get long term disability [6]. Aneurysm rupture can be prevented through angiographic imageries by using medical imaging methodologies to increase the visual observation with passage of time [7–10].

SAH mainly happens because of congenital defects braced by other hazardous situations like head trauma, high blood pressure, infection, and atherosclerosis. Aneurysm detection before rupture is much better than post-treatment [11]. Proper detection of CA is the most crucial task for most neurologists. Angiography is mostly used for the detection and diagnosis of cerebral aneurysm. Angiograms also help in detecting the size and location of aneurysms besides providing accurate visual information [12]. This information from angiograms provides the basis for the presented paper. Appropriate detection of aneurysms proved very beneficial in their prediction [13–15]. Substantial complications in precise detection of aneurysms from angiographic images are intensity-based inhomogeneity and poor contrast of blood vessels [16–19].

CA detection is used from different image modalities in order to find out the novel realm and is abundant to be discovered according to high accuracy and perfection results [20–24]. The most commonly used image modalities for the

[a] e-mail: nazeer@hanyang.ac.kr (corresponding author)

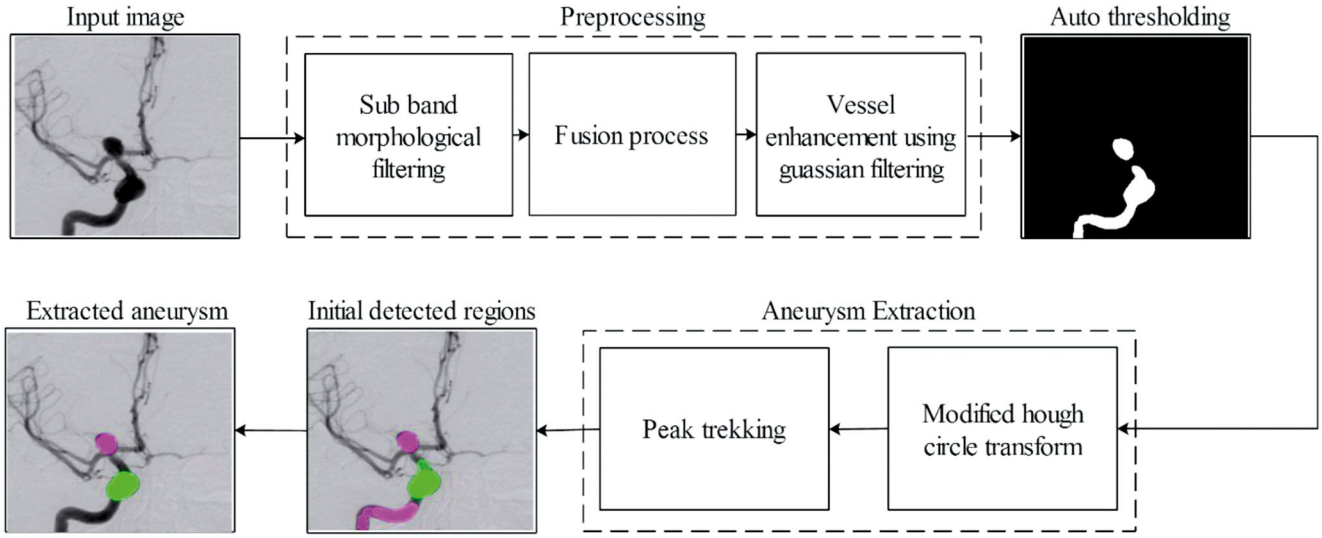

Fig. 1. Stages of the proposed methodology.

detection of CA are considered in magnetic resonance angiography (MRA), 2D digital subtraction angiography (2D-DSA), computed tomography angiography (CTA), and 3D X-ray rotational angiography (3D-RA) [25]. One detection algorithm that works for images acquired through datasets of the above techniques is initially anticipated [26–28]. However, that combination of 3D-RA with DSA is considered as the most subtle method for aneurysm detection [29]. However, the work presented by [30] claims that DSA is a feasible choice for countries that are still under development. Therefore, we use a global thresholding with peak trekking Hough transform approach for measuring CA using the DSA method. The proposed method does not only provide the salient information about the size of CA but also provides the sufficient category of CA to estimate the rupturing state.

Only limited approaches have been presented for the detection of CA in medical imageries [31]. Mostly all the presented methods rely on basic two-step strategies that first detect the possible areas based on segmented vasculature. For early findings of CA, three different approaches are used, which include: skeleton-based, shaped-base, and image difference-based methods, respectively [32–34]. For shape-based approaches a writhe numeral is used to discover irregularities in vasculature that could perhaps expose to aneurysms [35]. Skeleton-based approaches discover abnormal regions of arteries by subtracting normal image from ground truth dataset. Techniques based on image-difference used a subtraction of a normal model image from ground truth dataset to discover abnormal regions [36–39]. The other types of approaches are hybrid methods that use the combination of two or more techniques [40]. Most of the presented methods worked with MRA datasets, while few implemented the multi-model approach using CTA and 3D-RA imaging [41,42].

Aneurysms are categorized into different types depending upon their size, for example if the aneurysm size exceeds 25 mm diameter, such aneurysm is termed as giant or large aneurysm. Apart from single aneurysms, multiple aneurysms also exist in practical situations with an incidence rate of 20–30% [43].

The walls of blood vessel branches are weaker as compared to other areas, so mostly aneurysm develops in these sections. The weakness in artery walls might be by birth, hypertension, high blood pressure, and arteriosclerosis [44]. Diagnosis of CA comprises of CT-scan, MRI, cerebral angiograms, and cerebrospinal fluid test. SAH can be prevented at initial stages if detected earlier by controlling the cholesterol level and high blood pressure.

A clear vision of blood vessels and arteries from the background of dense soft and bony tissues is obtained through controlled management of radio-opaque regions [41]. This technique is termed as Digital Subtraction Angiography (DSA). It deducts post-opacification image from a pre-opacification image. DSA not only detects aneurysms, it also detects the presence of fatty plaque and blood clots that increase the risk of stroke and other malformations [32].

The paper has been arranged as follows: Section 2 describes the mathematical modeling of the proposed auto-thresholding algorithm and the entire technique is summarized. Parameter optimization is also discussed in the same section. Performance and simulation results of the proposed method are shown in sect. 3 followed by some conclusive remarks in sect. 4.

2 Mathematical modeling

We present a novel algorithm of sub-band morphological operation for retrieving salient information and auto-thresholding is used with the peak trekking (MHCT-PT) scheme in the Hough transform domain. CA classification is based on its severity state. The entire procedure is demonstrated in fig. 1.

Consider a patient having anatomic thickness of θ_t, vessel artery thickness of θ_l, and a coefficient of linear attenuation of δ_t. Formerly, the intensity of post-opacification also known as "live" and pre-opacification also known as "mask" is assumed as I_m, and I_I, correspondingly,

$$I_m = I_0 \xi^{-\delta_t \theta_t}, \tag{1}$$

$$I_I = I_0 \xi^{-(\delta_t \theta_t + (\delta_I \theta_I)}. \tag{2}$$

In the above equation, I_0 signifies the photon fluency without using any opacification. The digital subtracted image is then gained by subtracting the logarithmic function [25] of the live image from the mask image. The subtracted image is hence described as

$$\begin{aligned} S_{\log} &= \ln I'_m - \ln I'_I, \\ S_{\log} &= [-\delta_t \theta_t] - [-(\delta_t \theta_t + (\delta_I \theta_I)], \\ S_{\log} &= (\delta_I \theta_I). \end{aligned} \tag{3}$$

In the given equation, $S_{\log}$ represents the logarithmically subtracted image.

2.1 RGB DICOM to gray scale conversion

The DICOM image data follows the standard format to meet the demands of electronic media. This standard ensures the global intra-operability of the medical instrumentation [43].

The basics colors are defined by three components of the RGB system with receptive system $c_i(\partial_i)$ for $i \in \{\mathrm{R}, \mathrm{G}, \mathrm{B}\}$, such that R represents red, G green, B blue colors, respectively. The $c_i(\partial_i)$ is used for enhancing the angiogram information of the given data. Through the estimation of the luminance of the colored image, it is converted into a gray scale image c_i using eq. (4).

A three-dimensional volume is defined by handling the component values as conventional Cartesian coordinates in Euclidean space. This model is represented by a cube using non-negative values in a range of $\{0-1\}$. The three-dimensional coordinates of the given color are shown as the 3D structure edges. This approach permits computations of the color likeness of two given RGB structures by computing the distance between them in order to maintain the separation boundaries while preserving matching similarity among similar pixels,

$$\begin{aligned} d(\partial) &= c_1(\partial)R + c_2(\partial)G + c_3(\partial)B, \\ Y &= \int_{\mathbb{R}} c_i(\partial_i)\mathrm{d}\lambda, \end{aligned} \tag{4}$$

where $\tau_R = \frac{\mathcal{H}(\partial_i)+1}{\mathcal{H}(\partial_R)}$, $\tau_G = \frac{\mathcal{H}(\partial_i)+1}{\mathcal{H}(\partial_G)}$, and $\tau_B = \frac{\mathcal{H}(\partial_i)+1}{\mathcal{H}(\partial_B)}$. The entropy $\mathcal{H}$ estimates the point by point data content in the imageries. Higher estimations of $\mathcal{H}$ contain more extravagant points of interest and solid edges. The entropy $\mathcal{H}$ is characterized using

$$\mathcal{H} = -\sum_{i=0}^{N-1} \partial_i \log_2(\partial_i), \tag{5}$$

where $N = 2^n (n = 8\,\mathrm{bit})$ are diverse shades of the gray pixel values, while ∂_i is the likelihood of the dark scale i, and the coefficient predicts color perceptions.

2.2 Retrieving salient information

The wavelet transform (WT) is used as a great tool in contemporary mathematical advancement in order to treat the time domain and frequency domain signals, concurrently. Therefore, it is particularly beneficial for perceiving the significant changes in patterns with respect to time. For the detection of signal singularities, WT is considered as one of the best tools available in order to locate the singularity point. It is conceded using the help of local maxima [45]. On the contrary, WT allows approximation in terms of low frequencies and time details in terms of high frequencies, respectively. WT has been extensively used in the area of fault localization, specially detecting fault in shafts, gears, bearings, and beams [1,3,8]. WT has also been widely used as a crack indicator [46]. The amplitude standards of critical peaks and sub-critical peaks are utilized to provision the Artificial Neural Network (ANN), which in return diagnose the position and depth of cracks or faults in detection systems [26].

WT has additionally been used to analyze indented rotors in terms of transverse open split [45]. They contemplated the capability of the framework for the detection of joined faults of unbalance and shaft cracks. However, the main

concept of the WT usage in existing applications (*e.g.*, machinery crack and fault diagnosis) is still very rare. This is because of the fact that it is difficult to interpret visual results of WT, however, efforts are made to attain the desired features [10]. The symmetric wavelet is observed to maintain the influential effect in the analysis of singularity systems, for instance, it was additionally found to perform well on anti-symmetric wavelet with a narrow pulse-like approach: Daubechies family with higher-order, *e.g.*, db10 [27]. In particular, the maximum usage of cross-correlation coefficients in crack detection is computed by analyzing the fault signal and the various wavelet functions by considering the library of the optimal wavelets [46]. The Daubechies family, particularly the six-order Daubechies wavelet was utilized for crack recognition because of its demanding effect in that particular area [46].

In general, we can categorize WT into orthogonal, biorthogonal, and non-orthogonal. In spite of the fact that these wavelets share some common properties, where every wavelet decomposes a unique image and the inverse wavelet is used as a reconstruction technique have shown results in huge difference, amongst the wavelet fusion strategies. The desired wavelets from the above three general classes Daubechies (orthogonal), spline (orthogonal), and trous (non-orthogonal) are chosen as the scientific models to execute wavelet fusion strategies. Our goal is to take advantage of the orthogonality of WT to get a deeper understanding of the effect of proximal boundaries of brain vessels blobs while investigating the possibility of optimizing shrinkage-thresholding functions for better performance in order to impose sparsity constraints [46,47]. To that end, we consider a most relevant biorthogonal wavelet system (bior4.4) to evaluate the efficiency of the brain vessel image signal at high scale variation.

A biorthogonal wavelet system (bior4.4) is used to investigate the present high scale deviation of aneurysm data [45, 46]. The crucial information of aneurysm might be lost during the retrieving stage of salient information. This is performed by using a sub-band replacement morphological operation of the given Y in the wavelet domain: $\mathcal{W}(Y) = \{Y^{ll}, Y^{hl}, Y^{lh}, Y^{hh}\}$. In fact, the direct manipulation of Y using the morphological operation is leaded to develop ringing artifacts and causes to mislead the required information [27].

To retrieve precise information, the wavelet transform is applied to two of the morphological disks given as: $\mathcal{W}(Y_{m1}) = \{Y_{m1}^{(ll)}, Y_{m1}^{(hl)}, Y_{m1}^{(lh)}, Y_{m1}^{(hh)}\}$, and $\mathcal{W}(Y_{m2}) = \{Y_{m2}^{(ll)}, Y_{m2}^{(hl)}, Y_{m2}^{(lh)}, Y_{m2}^{(hh)}\}$. Where, Y_{m1} and Y_{m2} are two morphological operations that are employed on input image Y. However, the processed image $\mathcal{W}(Y_{m1})$ inclines a useful information of high frequency data but its low frequency information may be declined. Therefore, the decomposition of $\mathcal{W}(Y_{m1})$, the concept of low frequency information has been replaced with the Y. Only $Y_{m1}^{(ll)}$ is replaced by Y^{ll}. Its output yields the processed image $\mathcal{W}(\tilde{Y}_{m1})$ in the wavelet transform with Y^{ll}, $Y_{m1}^{(hl)}$, $Y_{m1}^{(lh)}$, and $Y_{m1}^{(hh)}$ using the inverse wavelet transform ($\mathcal{W}^{-1}$).

Similarly, the image Y_{m2} leads to determine the lower frequency data, and its high frequency data may be corrupted through NLM operation [22] by oversharpening of the high frequency data. Therefore, the wavelet transform of Y_{m2}, the higher information data have been replaced to the high frequency Y. Technically, $\mathcal{W}(\tilde{Y}_{m2})$ describes the four information sets given by $Y_{m2}^{(ll)}$, $Y_{m2}^{(hl)}$, $Y_{m2}^{(lh)}$, and $Y_{m2}^{(hh)}$. The last three information sets encompassed the high frequency information and they are substituted by the Y^{hl}, Y^{lh}, and Y^{hh}, respectively. In output the processed information in wavelet transform with subbands $Y_{m2}^{(ll)}$, Y^{hl}, Y^{lh}, and Y^{hh} are reconstructed using the inverse wavelet transform.

The primary image $\tilde{Y}_{m1}$ and $\tilde{Y}_{m2}$ must be fused with the provided image Y for matching the relevant data that may have been knocked out in the additional technique. In the following section, a fusion process is introduced for attaining the salient detail information of Y for keeping the significant detail data of Y by mixing up the $\tilde{Y}_{m1}$ and $\tilde{Y}_{m2}$.

2.3 Edge enhancement

Let us develop the combination of $\tilde{Y}_{m1}$ and Y by

$$\Psi_1 := \mu_{m1-1} \times \tilde{Y}_{m1} + \mu_{m1-2} Y, \tag{6}$$

where the weights μ_{m1-1} and μ_{m1-2} are chosen per (Shanon) entropy value of $\mathcal{H}$ and observed the given noise standard deviation $\widehat{\sigma}$ of Y. The $\mathcal{H}$ of $|\nabla\tilde{Y}_{m1}|$ and the $|\nabla\tilde{Y}_{m1}|$ is based on the gradient of the Sobel edge filter. The $\mathcal{H}$ determines the significant information in an image. The improved values of $\mathcal{H}$ prove richer in significant information [21]. If the $\mathcal{H}$ is high, $\tilde{Y}_{m1}$ is developed with technical data. Thus, a large value of the weight μ_{m1-1} has been assigned to $\tilde{Y}_{m1}$. If $\widehat{\sigma}$ is minimized, Y shows a large value of the weight μ_{m1-2}. This leads to the weights value as follows:

$$\mu_{1\tilde{G}} = \frac{2Hlog_2(\widehat{\sigma}+1)}{M}, \qquad \text{and} \qquad \mu_{2\tilde{G}} = 1 - \mu_{1\tilde{G}}, \text{ such that } 0 \leq \mu_{1\tilde{G}},\ \mu_{2\tilde{G}} \leq 1.$$

Technically, by considering the combination of $\tilde{Y}_{m2}$ and Y using

$$\Psi_2 := \mu_{m2-1} \times \tilde{Y}_{m2} + \mu_{m2-2} Y, \tag{7}$$

the weights μ_{m2-1} and μ_{m2-2} are well defined in terms of $\tilde{Y}_{m2}$ and the noise standard has been deviated $\widehat{\sigma}$ as in eq. (7).

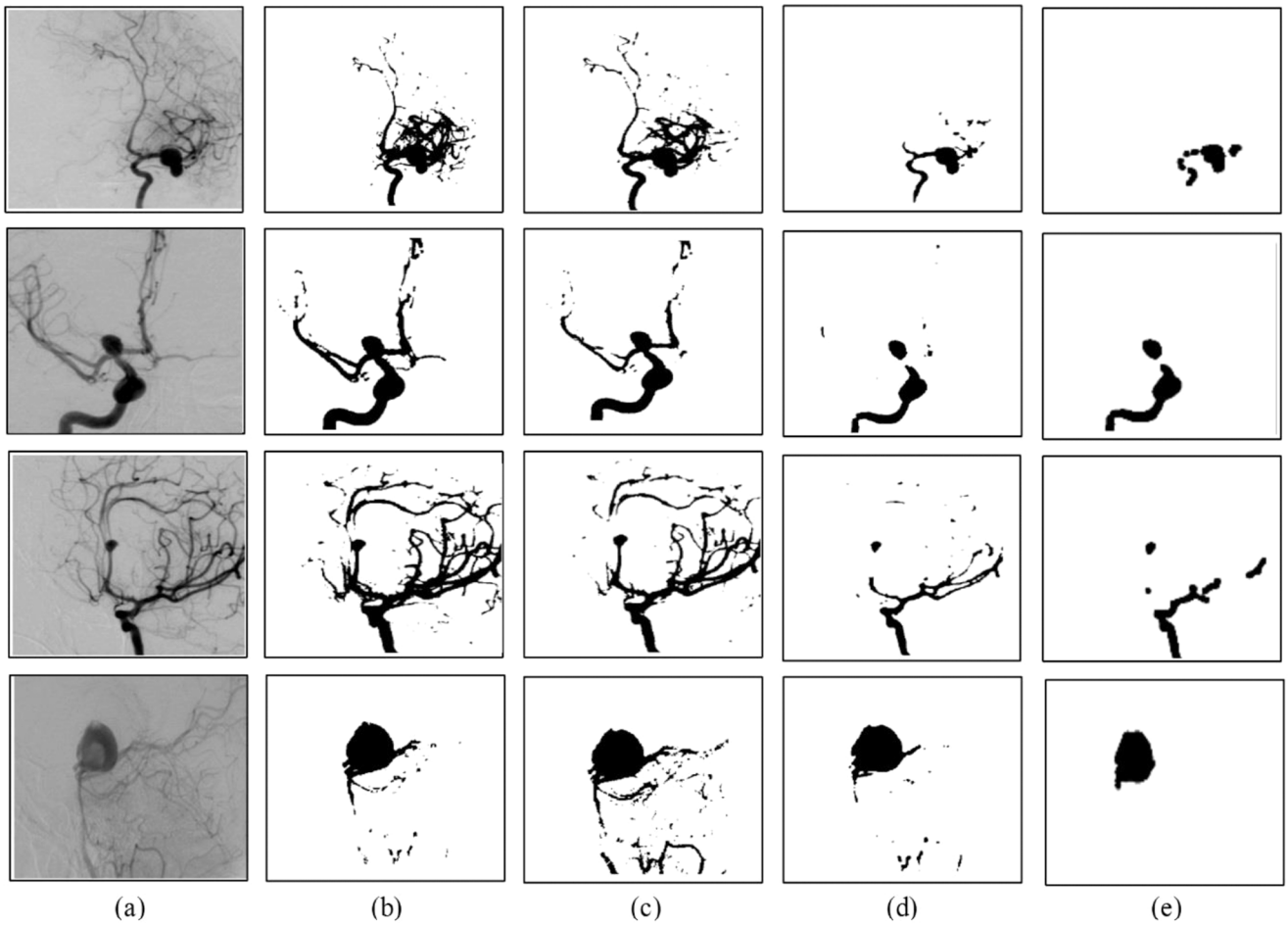

Fig. 2. Test images 1–4 (a) original image (true image); (b) Sauvola's threshold method; (c) Otsu's threshold method; (d) Jubin *et al.*; (e) proposed method.

We consider the given images Ψ_1 and Ψ_2 in processed data at second stage. Finally, in the pre-processed image Y, the NLM operation is employed to Ψ_1 and Ψ_2, respectively, in order to refine the images $\widetilde{\Psi}_1$ and $\widetilde{\Psi}_2$ followed by a fusion process:

$$\Phi := \widetilde{\Psi}_1 + \widetilde{\Psi}_2. \tag{8}$$

A trade-off has been considered between $\widetilde{\Psi}_1$ and $\widetilde{\Psi}_2$, where $\mu_{1\tilde{G}}$ and $\mu_{2\tilde{G}}$ are calculated using the terms $\widetilde{\Phi}$ and $\widetilde{\Psi}$. The Φ is the final stage processed in order to be used as an input in the process of second step thresholding. The radius of the blood vessel is predicted through deviation of smoothing Gaussian kernel. It is regarded as the most vital preprocessing phase for enhancement as it eliminates the background noise and highlights the vessel structure [48].

2.4 Auto-thresholding

The threshold for the image is estimated as follows:

$$\Delta(\alpha,\beta) = \begin{cases} I_\lambda & F(\alpha,\beta) < \lambda, \\ I_\lambda : & F(\alpha,\beta) \geq \lambda, \end{cases} \tag{9}$$

where λ is evaluated as

$$\lambda = \min\left[\overset{\forall}{}_{(\alpha,\beta)\in(X\times Y)} F(\alpha,\beta)\right] + \max\left[\overset{\forall}{}_{(\alpha,\beta)\in(X\times Y)} \omega(\alpha,\beta)\right].$$

Auto-thresholding is applied on the binary images obtained from the grayscale DICOM imageries. This hasperceived that the proposed method clearly extracts the clear region of interest in comparison with the listed methods.

Figure 2 shows the qualitative results of the proposed algorithm with the listed methods. The auto-threshold image [49] is compared with the most extensively used thresholding algorithms like Sauvola's threshold [34], Otsu's threshold [38], and Jubin *et al.* [9] methods. Sauvola's edge is generally referred to as a thresholding as locally adaptive with nearby binarization benchmark approach of 94.9%. Moreover, Otsu's method has been referred to widely to consider the global thresholding system.

2.5 Space discretization to precise detection

The importance of the midpoint circle algorithm is proven to be one of the effective methods for calculating the position of pixels that are around a circular path. These pixels are centered at coordinates (0, 0) having a radius r. The engendered circle is shifted to the appropriate position of the screen by moving its center to $(r_c,\ y_c)$. The computed circular section is broken down into eight point's symmetric regions, because of its regularity in nature. The key concept of the slope of the curve varies from 0 to 1 in the first octant of the given circular region. So, over this octant, unit steps can be taken in the direction of positive x-axis location and the decision parameters are predicted to the closeness of two possible y positions of the circular path. In this connection, a circular function $f_{\text{circle}}(\alpha, \beta)$ is defined as

$$f_{\text{circle}}(\alpha, \beta) = \alpha^2 + \beta^2 - \gamma^2. \tag{10}$$

To find the relative location of any point $(x,\ y)$ with key concept to the circular boundary has been determined by considering the polarity function. If $f_{\text{circle}}(\alpha, \beta) > 0$ it has been shown that $(\alpha,\ \beta)$ is inside the circlular boundary, $f_{\text{circle}}(\alpha, \beta) = 0$ shows that $(\alpha,\ \beta)$ is on the circle boundary, and if $f_{\text{circle}}(\alpha, \beta) < 0$ it shows that $(\alpha,\ \beta)$ is outside the circle boundary. Let us assume that pixel $(x_k,\ y_k)$, is plotted, the next position pixels are plotted followed by the parameter (p_k), with the position of the pixels, *i.e.*, $(\alpha_k + 1,\ \beta_k)$ and $(\alpha_k + 1,\ \beta_k - 1)$. This decision about the given parameter (p_k) is evaluated for the circular function between these pixels as

$$p_k = f_{\text{circle}}\left((\alpha_k + 1)^2, (\beta_k - \frac{1}{2})^2 - r^2\right). \tag{11}$$

The next pixel to be selected $(x_{k+1},\ y_{k+1})$ depends on the p_k sign as

$$\beta_{k+1} = \begin{cases} \beta_{k-1} & \text{when} \quad p_k \leq 0, \\ \beta_k & \text{when} \quad p_k < 0. \end{cases} \tag{12}$$

Successive decision parameters (p_{k+1}) can easily be attained through incremental calculations by assessing the circle function repeatedly. A recursive expression of the next decision parameter from the current one is

$$\begin{aligned} p_k + 1 &= f_{\text{circle}}\left(\alpha_{k+1} + 1, \beta_{k+1} - \frac{1}{2}\right), \\ &= \left(((\alpha_k + 1) + 1)^2 + \left(\beta_{k+1} - \frac{1}{2}\right)^2 - \gamma^2\right), \\ &= p_k + 2(\alpha_k + 1) + \left(\beta_{k+1}^2 - \beta_k^2\right) - (\beta_{k+1} - \beta_k) + 1. \end{aligned} \tag{13}$$

The decision parameters at initial stage are selected by assessing the circular function at initial location $(\alpha_0, \beta_0) \equiv (0, \gamma)$ given as

$$\begin{aligned} p_0 &= f_{\text{circle}}\left(1, \gamma - \frac{1}{2}\right), \\ &= 1 + \left(\gamma - \frac{1}{2}\right)^2 - \gamma^2. \end{aligned} \tag{14}$$

Some mathematical notations should be introduced before presenting the Hough hierarchy:

$$f_{\text{circle}}^r(x - x_c, y - y_c) = (x - x_c)^2 + (y - y_c)^2 - r^2, \tag{15}$$

where $f_{\text{circle}}^r(x - x_c, y - y_c)$ represents the circle function with the center at point $(x_c,\ y_c)$ with radius r. Points which lie on the interior of the annular region confined by radius r_1 and r_2, respectively, are assumed as

$$\delta\Omega_r(x_c, y_c) = \left\{(x, y) \in (X \times Y) :\ f_{\text{circle}}^r(x - x_c, y - y_c) = 0\right\}. \tag{16}$$

Given that $\{0 \leq r_1 \leq r_2\}$, in order to map the required pixels of a binary image Δ to a 3D parameter space the mapping function for the modified space discretization algorithm is well defined as

$$v(\alpha,\beta) = \sum_{r=1}^{\rho} \left\lceil \frac{|\delta\Omega_r(\alpha,\beta) \cap \Delta|}{\delta\Omega_r(\alpha,\beta)} \right\rceil. \tag{17}$$

In the above equation, operator $||$ represents the set cardinality that is obtained to obtain the desired number of pixels, while $\lceil\cdot\rceil$ is used as a ceiling operator. Hough hierarchy $\mathbf{H}$ has been generated by casted votes. This adjustment for all the pixel positions is noticed within the provided image, by the relation

$$\rho = \left\{(\alpha,\beta) \in (X \times Y) : \cup_{\forall(\alpha,\beta)} v(\alpha,\beta)\right\}. \tag{18}$$

The co-domain of the function $v(x,y)$ and upper limit of the relation ρ is demonstrated through eqs. (27) and (28), respectively, as

$$V = \{0,1,2,\ldots,\mathbf{H}\}, \quad \text{where as} \quad v(\alpha,\beta) \in V, \tag{19}$$

$$\max(\rho) = \{(\alpha,\beta) \in (X \times Y), v(\alpha,\beta) \in \rho : \max[v(\alpha,\beta)]\}. \tag{20}$$

The graph developed of ρ, has a ternary combination among X, Y and V, as will be shown in eq. (30):

$$\rho : X \times Y \rightarrow V, \tag{21}$$

$$X \times Y \times V = \{(\alpha,\beta,v(\alpha,\beta)) : \alpha \in X \wedge \beta \in Y \wedge v(\alpha,\beta) \in V\}. \tag{22}$$

2.6 Peak trekking

The key concept of the Hough hierarchy is followed the 3D parameter space that looks like a mountain range, so it should be discovered like an excursion hence, termed as peak trekking. The 3D local mountain from the mountain range (3D parameter space) is performed to detected the regions of the binary image [45]. The very first step for the detection of aneurysms is to get the location of the utmost peak and to store the first position of array C_1,

$$C_1 = \{(\alpha,\beta) \in (X \times Y) : \rho(\alpha,\beta) \cap \max(\rho) \wedge |\rho(\alpha,\beta) \cap \max(\rho)| = 1. \tag{23}$$

The above equation shows that even if many points satisfy the condition, only one will be considered. A circular region having center C_1 with radius r_{out} is drawn as

$$R_1 = \left\{(\alpha,\beta) \in (X \times Y) : \Omega^{-}_{r_{\text{out}}}(C_1)\right\}. \tag{24}$$

In Ω^{-}_{r}, "$-$" sign indicates that points lie within the annular region instead of the exterior region. The very next step is to find out pixels positions lying inside the annular region having center C_1 bounded by the inner and outer radius of $r_{\text{in}} - 1$ and $r_{\text{out}} - 1$, respectively. These positions once assessed are stored in the second position of array C. In this situation, radii of boundary are abridged by 1, which specifies a unit level decrement along dimension V of parameter space.

Equations (22) to (24) can be generalized using principle of mathematical induction, through recursive relation as shown in eqs. (25) and (26). Except for level 1, where C_1 is already defined by eq. (23),

$$C_n = \begin{cases} \{(\alpha,\beta) \in (X \times Y) : [r_{\text{in}} - (n-1)]\Omega^{-}_{[r_{\text{out}}-(n-1)]}(C_{n-1})\} & : n > 1, \\ \{(\alpha,\beta) \in (X \times Y) : \rho(x,y) \cap \max(\rho) \wedge |\rho(\alpha,\beta) \cap \max(\rho)| = 1 & : n > 1, \end{cases} \tag{25}$$

$$R_n = \left\{(\alpha,\beta) \in (X \times Y) : 0\Omega^{-}_{r_{\text{out}}-1}(C_n)\right\}. \tag{26}$$

In the given equation n defines the level number. From the given equation, n circular region is generated which superimposed to give first detected regions. Detected region D_1 is given demonstrated as

$$D_1 = \cup_{n=1}^{\max(\rho)-\Theta} R_n. \tag{27}$$

D_1 represents the first detected region which is then subtracted from Hough hierarchy ρ from averting redundancy in detected regions,

$$\rho = \rho \cap \overline{D_1}. \tag{28}$$

Region detection and subtraction is continuing to iterate until and unless the condition $\max(\rho) \geq PeakDepth$ is desecrated which is responsible for deciding the height of post processed ρ. 3D parameter space is considered enough

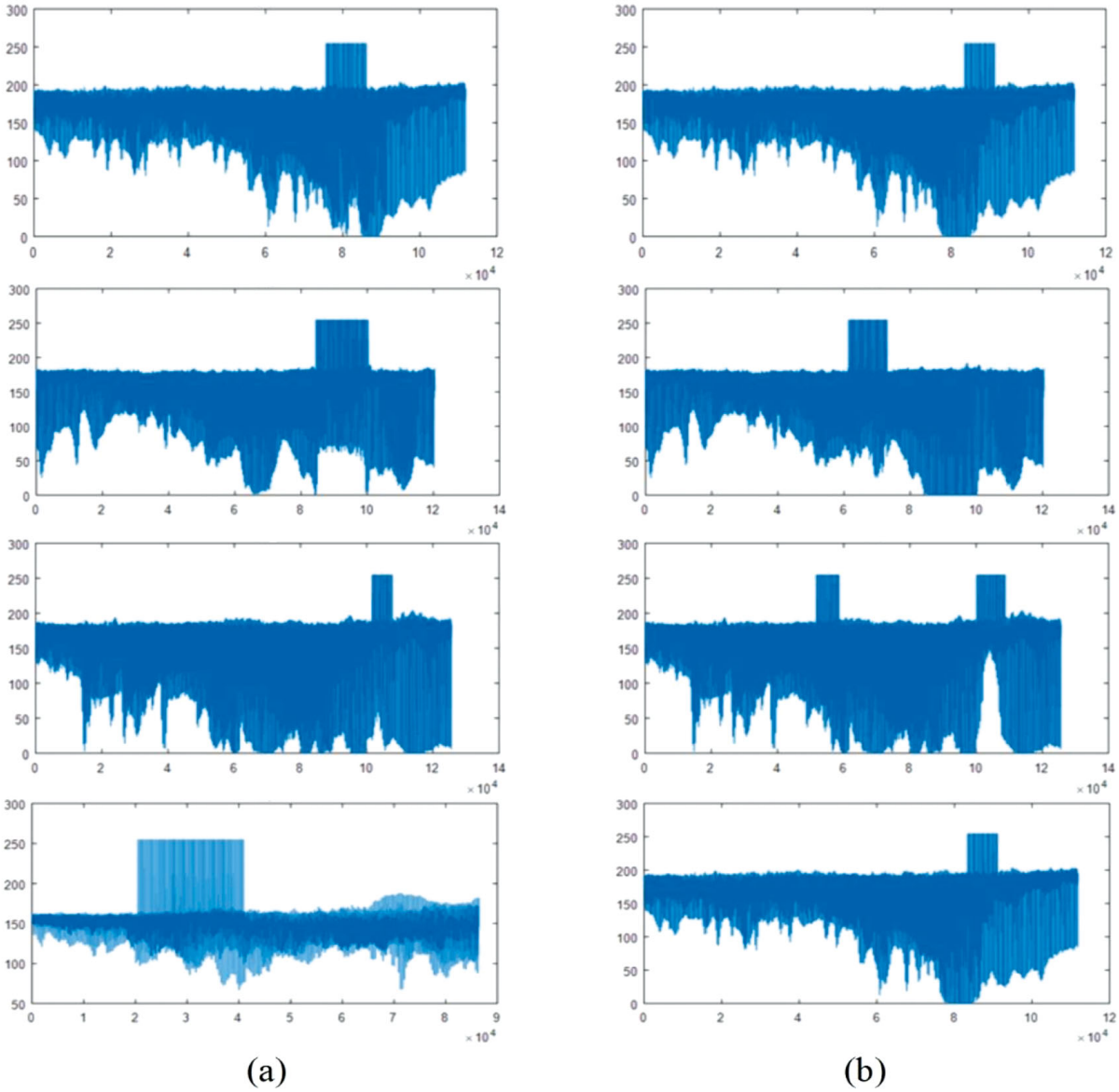

Fig. 3. 1D plot information on test images: (a) Jubin *et al.* [9] and (b) the proposed method.

for regions called as mountains. Condition for $\max(\rho) \geq PeakDepth$ is $\rho = \rho \cap \overline{D_{n_p}}$, in which the variable n_p denotes the peak number, which acts like a filter for noisy shape. A unique ID for detecting, maintaining the index for such regions. n_p is responsible for maintaining the FIFO principle for retaining hierarchy information. Thus, initial detected regions can be seen as follows:

$$n_p \in N_p, N_p = \left\{1, 2, ..n_p^{\max}\right\}, \tag{29}$$

where $n_p^{\max}$ represents initially detected regions. Finally, accurate detected regions are given as follows:

$$D = \{n_p \in N_p : D_{n_p}\}. \tag{30}$$

Figure 3 shows the 1D plot information of the Jubin *et al.* [9] method and proposed methodology respectively. Notice from fig. 3 that the graph peaks of the proposed method are shrinked with higher accuracy in order to localize the affected position than that of the listed method. This happens because the proposed method follows the exactness of the affective area to confine the computed region with much higher accuracy.

Algorithm 1.

Input: DICOM Image ($\boldsymbol{Y}$)
1. $\boldsymbol{f}$ – sub band morphological operation ($\boldsymbol{Y}$)
2. $\boldsymbol{\zeta}$ – Min ($\boldsymbol{f}$)
3. $\boldsymbol{\Upsilon}$ – Sobel ($\boldsymbol{f}$)
4. $\boldsymbol{\sigma}$ – max ($\boldsymbol{\Upsilon}$)
5. $\boldsymbol{\lambda}(\textit{Thresholding}) - (\boldsymbol{\zeta} + \boldsymbol{\sigma})$
6. Get circle hierarchy $\boldsymbol{\delta} - (\boldsymbol{\lambda}, \text{Hough Hierarchy}(\boldsymbol{\rho}))$
7. Detect initial regions ($\boldsymbol{\delta}$)
Output: A = Aneurysm regions ($\boldsymbol{\delta}$)

2.7 Aneurysm detection

Neurologists suggest circular shape and diameter size as significant features for the detection of cerebral aneurysms. Three features are considered for the detection of aneurysms: peak number, shape type, and compactness factor. The peak number is represented as n_p and indicates the shape convexity. The area and the compactness factor of the detected shape for a particular n_p is calculated by counting the number of pixels present within the shape as follows:

$$A_{D_{n_p}} = \sum_{\forall(x,y)} D_{n_p}, \tag{31}$$

$$C_{D_{n_p}} = \frac{4\pi A_{D_{n_p}}}{P^2_{D_{n_p}}}\,. \tag{32}$$

In the given equation, $A_{D_{n_p}}$ and $P_{D_{n_p}}$ indicates the area and perimeter of the detected shape correspondingly, for a specific peak number. If $C_{D_{n_p}}$ is observed close to 1 then it is assumed to be circular, however if it is noticed close to 0 it designates a rectangular or tubular structure. This constraint has provided a very useful discrimination for normal and aneurysms cells.

The queue of generated shapes may contain different size aneurysms, arteries, vessels, and background noises [9]. Consequently, it is crucial to separate these portions from other detected shapes. Aneurysms detection depends on three conditions, such: $A_{D_{n_p}} \geq Minimum\ area$, while the minimum area is demonstrated as follows:

$$Minimum\ area = 100 \times \left\lfloor \frac{A_{\boldsymbol{D}_1}}{100 \times k} \right\rfloor. \tag{33}$$

In the above given equation A_{D_1} represents shape area (D_1), that is produced by peak number 1, *i.e.* ($n_p = 1$), condition 2 represents optimized weights, and condition 3 is true for shape D_{n_p}. If condition 1, 2, and 3 are estimated to be true for shape $D_{n_p} - 1$. In this situation, condition 1 and 2 are essential for the detection of cerebral aneurysms. However, condition 3 is most crucial and enough for the proposed algorithm.

The adjustable parameters of the presented algorithm include: hierarchy height, neighborhood depth, peak depth, C, and k. Multiparameter optimization is a problem here, so the significant parameter turns out to be a neighborhood depth. For performance evaluation of the algorithm, segmentation results were compared to a ground truth image using three performance metrics which are: sensitivity, accuracy and specificity. In practical situations, the segmented image based on the manual approach is leaded to error on applying the skilled human observation and interpretation of the given pixels [45,46,50]. Most appropriate detection will have values of sensitivity and specificity equal to one, while most algorithms fall short of ideal. The optimum value for sensitivity and specificity is observed to be 1.

The aim of this research is to precisely detect the aneurysm regions in DICOM images obtained through DSA. A metric for accuracy measurement of aneurysm detected regions is presented [30]. Manually segmented ground truth regions δ are considered and their Euclidean distance transforms (Θ) are computed. Distance is normalized $\delta_{\xi n}$ and with these segmented aneurysm regions $\mathbb{A}$, the percentage of common pixels is computed.

$$\delta_\xi = \Theta(\delta),$$

$$\delta_{\xi_n} = \frac{\delta_\xi}{\max(\delta_\xi)}\,,$$

$$Accuracy\ (\%) = \frac{\delta_{\xi_n} \wedge \mathbb{A}}{\delta} \times 100.$$

In the above equation, $\wedge$ is implemented using max operation. As thresholding safely measures aneurysm regions maintain a safe boundary of these regions without affecting overall accuracy of detection, there is no need for the measurement of overflow percentage.

Table 1. Classification of patients with cerebral aneurysms at early diagnostic stage.

Grade	Criteria	Number of CA	Deaths
I	Minor headache	61	7
II	Severe headache	88	23
III	Drowsiness	79	29
IV	Severe hemiparesis	35	25
V	Deep coma	12	12

Table 2. Classification and detection for 1st test image.

Area	Compactness factor	Peak number	Aneurysm?	Diameter (mm)	Type of aneurysm
793	0.64	1	True	19.07	Large
350	0.61	2	True	12.67	Medium
222	0.43	3	False	10.09	–
157	0.43	4	False	8.48	–
209	0.47	5	False	9.79	–

Table 3. Classification and detection for 2nd test image.

Area	Compactness factor	Peak number	Aneurysm?	Diameter (mm)	Type of aneurysm
1496	0.64	1	True	17.46	Large
711	0.62	2	True	12.04	Medium
958	0.35	3	False	13.97	–
287	0.62	4	False	7.65	–
248	0.55	5	False	7.11	–

Table 4. Classification and detection for 3rd test image.

Area	Compactness factor	Peak number	Aneurysm?	Diameter (mm)	Type of aneurysm
289	0.65	1	True	5.75	Small
315	0.68	2	True	6.01	Small
194	0.69	3	True	4.71	Small
584	0.36	4	False	8.18	–
348	0.45	5	False	6.31	–

Table 5. Classification and detection for 4th test image.

Area	Compactness factor	Peak number	Aneurysm?	Diameter (mm)	Type of aneurysm
2587	0.60	1	True	34.44	Giant
168	0.52	2	False	8.78	–

Table 6. Performance analysis of the proposed technique.

Test image	Sensitivity	Specificity	Accurate match (%)	
			Jubin *et al.* [9]	Proposed method
1st	100%	100%	99.0094	99.8173
2nd	100%	100%	95.9682	98.5273
3rd	100%	100%	93.9899	98.9435
4rth	100%	100%	98.0625	99.5806

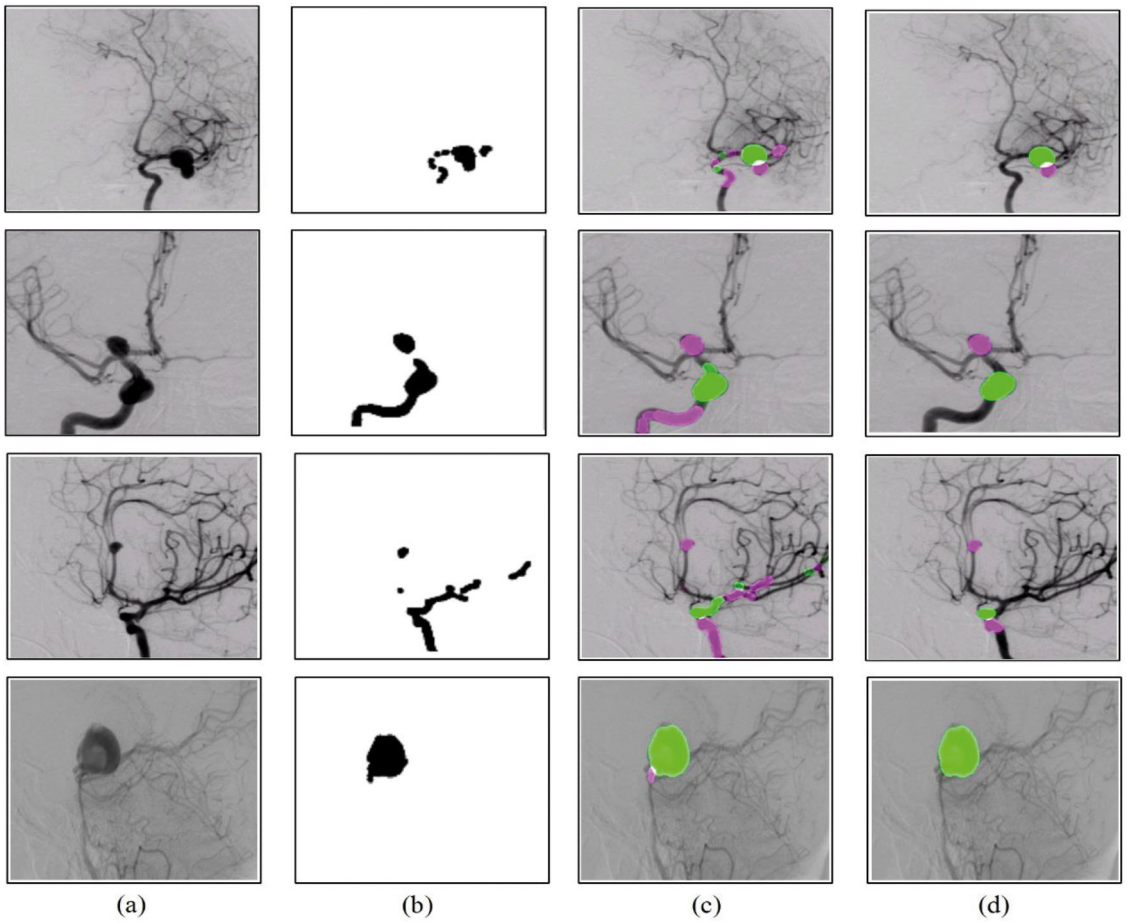

Fig. 4. Detection of cerebral aneurysms for test images 1–4.

Table 7. Comparison of the proposed method with the listed methods.

Reference	Sensitivity	Specificity	Accuracy	User interaction	Modality
Proposed method	1	1	99.2	Automatic	DSA
[8]	1	1	96.9	Automatic	DSA
[6]	0.99	1	99.4	User interactive	DSA
[7]	0.99	1	99.5	User interactive	DSA
[5]	0.974	0.9	95.8	Semi-automatic	Multi section CT Angiography
[4]	0.95	–	–	Automatic	3D-RA, MRA, CTA

3 Results and discussion

We have tested our algorithm on text images of various types and size of aneurysms to exhibit the performance of the proposed algorithm. Test images for experimental evaluation are taken from the benchmark database of Dr. Balaji Anvekar's neurology cases [42] and brain aneurysm foundations [43]. The simulations were performed on MATLAB R2018a software. The results of the proposed algorithm for properly locating the position and size of the aneurysm are shown in fig. 4. In each of these imageries, the actual input image obtained through DSA Image (Y) is shown in fig. 4(a). This gray scale image (Y) is segmented into binary image (Δ) using the proposed auto-thresholding method as shown in sub-figure (b). Detected regions ($\mathbb{D}$) generated from peak trekking with increasing the peak number (n_p) over the input image are shown in fig. 4(c). Figure 4(d) shows the aneurysms regions ($\mathbb{A}$) are detected and classified through detected regions ($\mathbb{D}$). Detection and classification of aneurysm regions are shown in tables 1, 2 3, 4 and 5 using parameters: peak number, area, compactness factor, and diameter.

It can be seen from both qualitative and quantitative analysis that the proposed algorithm has a descent ability to detect and classify the affected regions. However, it does not contain only a single region but also multiple aneurysms. It can be observed from the processed images as shown in fig. 4 and performance analysis is demonstrated in table 6. This shows that the proposed algorithm is capable enough for finding the accurate type of the affected region and the proper boundary of the detected aneurysm. Tables 2 to 5 present the detection and classification of single and multiple aneurysms based on four parameters. The proposed algorithm is successful in detecting the type and proper location of aneurysms with a much higher accuracy rate. We have compared our proposed approach with different state of the art methods in the literature as shown in table 7. Inspired by the work of Jubin *et al.* [9] different parameters like sensitivity, specificity, and accuracy have been used to evaluate the performance of the proposed system. The given table shows that the proposed algorithm achieves a higher accuracy compared with the Jubin *et al.* [9] automatic method. It was observed in Li *et al.* [7] and Villablanca *et al.* [8] about higher accuracy results; however in these methods the sensitivity value was supposed less than 1 in order to maintain the tradeoff between sensitivity and accuracy value.

The proposed method achieves higher accuracy as compared to earlier methods in terms of both specificity and sensitivity. Optimum selection of these values can lead to accurate detection of any type of aneurysms and even abnormal vessels. Moreover, the proposed method is very efficient in emphasizing the affected area with great accuracy.

4 Conclusion

Successful detection of cerebral aneurysms is achieved using the novel sub-band morphological operation method. Peak trekking of the Hough hierarchy is calculated from these auto-thresholded grayscale images in order to observe the weak spots in blood vessels. This helps to manage the critical situation of patients by observing the sac-like structures in clear and in a short span of time. The proposed method using the morphological operation in the wavelet domain is not only helpful to save precious human lives, it also decreases the time duration to locate the abnormal vessels. This leads to an optimum selection of the problematic values for an accurate detection of types of aneurysms and abnormal vessels.

List of abbreviations.

Acronym	Definition
CA	Cerebral aneurysm
CTA	Computed tomography angiogram
DSA	Digital subtraction angiography
SAH	Subarachnoid hemorrhage
LDA	Linear discriminant analysis
MRI	Magnetic resonance imaging
DICOM	Digital imaging and communications in medicine
ROI	Region of interest
MHCT	Modified hough circle transform
WT	Wavelet transform

References

1. Clemens M. Hentschke, Oliver Beuing, Rosa Nickl, Klaus D. Tönnies, *Automatic cerebral aneurysm detection in multimodal angiographic images*, in *Nuclear Science Symposium and 2011 IEEE Medical Imaging Conference (NSS/MIC)* (IEEE, 2011) pp. 3116–3120.
2. Eelco F.M. Wijdicks, David F. Kallmes, Edward M. Manno, Jimmy R. Fulgham, David G. Piepgras, Mayo Clin. Proc. **80**, 550 (2005).
3. C.M. Strother, F. Bender, Y. Deuerling-Zheng, K. Royalty, K.A. Pulfer, J. Baumgart, M. Zellerhoff, B. Aagaard-Kienitz, D.B. Niemann, M.L. Lindstrom, Am. J. Neuroradiol. **31**, 919 (2010).
4. William E. Hunt, Robert M. Hess, J. Neurosurg. **28**, 14 (1968).
5. Clemens M. Hentschke, Oliver Beuing, Rosa Nickl, Klaus D. Tönnies, SPIE Med. Imag. Int. Soc. Opt. Photon. **8315**, 83151I (2012).
6. A.M. McKinney, C.S. Palmer, C.L. Truwit, A. Karagulle, M. Teksam, Am. J. Neuroradiol. **29**, 594 (2008).
7. Li Lu, Long Jiang Zhang, Colin S. Poon, Sheng Yong Wu, Chang Sheng Zhou, Song Luo, Mei Wang, Guang Ming Lu, Radiology **262**, 605 (2012).

8. J. Pablo Villablanca, Reza Jahan, Parizad Hooshi, Silvester Lim, Gary Duckwiler, Aman Patel, James Sayre *et al.*, Am. J. Neuroradiol. **23**, 1187 (2002).
9. Jubin Mitra, Abhijit Chandra, Tanmay Halder, ELCVIA **12**, 57 (2013).
10. Muhammad Nazeer, Nargis Bibi, Adnan Jahangir, Zahid Mahmood, Pattern Anal. Appl. **21**, 1013 (2018).
11. Jeffrey C. Weinreb, Paul A. Larson, Pamela K. Woodard, William Stanford, Geoffrey D. Rubin, Arthur E. Stillman, David A. Bluemke, Andre J. Duerinckx, N. Reed Dunnick, Geoffrey G. Smith, Radiology **235**, 723 (2005).
12. Dan L. Longo, Anthony S. Fauci, Dennis L. Kasper, Stephen L. Hauser, J. Larry Jameson, Joseph Loscalzo, in *Harrison's Principles of Internal Medicine 18E*, Vol **2 EB** (McGraw Hill Professional, 2012).
13. G.B. Bradac, *Cerebral Angiography: Normal Anatomy and Vascular Pathology* (Springer-Verlag, 2011).
14. Mehmet. Sezgin, J. Electron. Imaging **13**, 146 (2004).
15. Jubin Mitra, Abhijit Chandra, *Detection of cerebral aneurysm by performing thresholding-spatial filtering-thresholding operations on digital subtraction angiogram*, in *Advances in Computing and Information Technology* (Springer, 2013) pp. 915–921.
16. Peter Mildenberger, Marco Eichelberg, Eric Martin, Eur. Radiol. **12**, 920 (2002).
17. Nazeer Muhammad, Nargis Bibi, IET Image Process. **9**, 795 (2015).
18. Zahid Mahmood, Tausif Ali, Nazeer Muhammad, Nargis Bibi, I. Shahzad, S. Azmat, KSII Trans. Internet Inf. Syst. **11**, 6069 (2017).
19. Nazeer Muhammad, Nargis Bibi, Adnan Jahangir, Zahid Mahmood, Pattern Anal. Appl. **21**, 1013 (2018).
20. V.C.P. Hough, *Method and means for recognizing complex patterns*, U.S. Patent 3,069,654, issued December 18, 1962.
21. Nazeer Muhammad, Nargis Bibi, Zahid Mahmood, Tallah Akram, Syed R. Naqvi, PloS ONE **12**, e0176979 (2017).
22. Nazeer Muhammad, Nargis Bibi, I. Qasim, Adnan Jahangir, Zahid Mahmood, Pattern Anal. Appl. **21**, 997 (2018).
23. Nazeer Muhammad, Nargis Bibi, Abdul Wahab, Zahid Mahmood, Tallah Akram, Syed R. Naqvi *et al.*, Comput. Electr. Eng. **70**, 413 (2018).
24. Mehreen Irshad, Nazeer Muhammad, Muhammad Sharif, Musarat Yasmeen, Eur. Phys. J. Plus **133**, 148 (2018).
25. Qiang Li, Shusuke Sone, Med. Phys. **30**, 2040 (2003).
26. Alejandro F. Frangi, Wiro J. Niessen, Koen L. Vincken, Max A. Viergever, *Multiscale vessel enhancement filtering*, in *International Conference on Medical Image Computing and Computer-Assisted Intervention* (Springer, Berlin, Heidelberg, 1998) pp. 130–137.
27. Naseer Ahmed, Daniele Linardi, Nazeer Muhammad, Cristiano Chiamulera, Guido Fumagalli, Livio San Biagio, Mebratu A. Gebrie, Muhammad Aslam, Giovanni Battista Luciani, Giuseppe Faggian, Front. Pharmacol. **8**, 645 (2017).
28. Jaakko Sauvola, Matti Pietikäinen, Pattern Recog. **33**, 225 (2000).
29. Nobuyuki Otsu, IEEE Trans. Syst. Man, Cybernet. **9**, 62 (1979).
30. Mark S. Nixon, Alberto S. Aguado, *Feature Extraction & Image Processing for Computer Vision* (Academic Press, 2012).
31. Cecilia Di Ruberto, Int. J. Comput. Appl. **48**, 19 (2012).
32. Xing Chen, Ling Lu, Yang Gao, *A new concentric circle detection method based on Hough transform*, in *2012 7th International Conference on, Computer Science & Education (ICCSE)*, (IEEE, 2012) pp. 753–758.
33. Olivier Ecabert, Jochen Peters, Hauke Schramm, Cristian Lorenz, Jens von Berg, Matthew J. Walker, Mani Vembar *et al.*, IEEE Trans. Med. Imaging **27**, 1189 (2008).
34. Luciano da Fona Costa, Roberto Marcond Cesar Jr., *Shape Classification and Analysis: Theory and Practice*. (CRC Press, 2009).
35. Donald D. Hearn, M. Pauline Baker, Warren Carithers, *Computer Graphics with Open GL* (Prentice Hall Press, 2010).
36. N. Muhammad, S. Khalid, M. Sharif, *An Automatic Measurement of the Traffic Sign with Digital Segmentation and Recognition*, in *IET Intelligent Transport Systems* (2018). `https://doi.org/10.1049/iet-its.2018.5223`.
37. Bushra Mughal, Muhammad Sharif, Nazeer Muhammad, Tanzila Saba, Microscopy Res. Techn. **81**, 171 (2018).
38. Nazeer Muhammad, Muhammad Sharif, Javeria Amin, Riffat Mehboob, Nargis Bibi, Naseer Ahmed, Front. Pediatr. **6**, 6 (2018).
39. Syed R. Naqvi, Tallah Akram, S. Iqbal, Sajjad A. Haider, Muhammad Kamran, Nazeer Muhammad, Appl. Nanosci. F **8**, 89 (2018).
40. Tze-Wey Loong, BMJ **327**, 716 (2003).
41. Bushra Mughal, Muhammad Sharif, Nazeer Muhammad, Eur. Phys. J. Plus **132**, 266 (2017).
42. Shabieh Farwa, Nazeer Muhammad, Tariq Shah, Sohail Ahmad, 3D Res. **8**, 26 (2017).
43. *Dr. Balaji Anvekar's Neuroradiology Cases*, in *Neuroradiology cases*, `http://www.yousaytoo.com/aneurysm-dsa/1896957`.
44. Zahid Mahmood, Nazeer Muhammad, Nargis Bibi, Yasir M. Malik, Naseer Ahmed, Inform. Med. Unlocked **13**, 9 (2018).
45. N. Muhammad, Z. Jehangiri, O. Hanif, S. Khattak, IET Intel. Transp. Syst. (2018) `https://doi.org/10.1049/iet-its.2018.5021`.
46. L.E. Goerge, B.A. Sultan, *The Use of Biorthogonal Wavelet, 2D Polynomial and Quadtree to Compress Color Images* (Berlin, Heidelberg, 2011) pp. 379–390.
47. M. Gómez, C. Castejón, J. García-Prada, Algorithms **9**, 19 (2016).
48. Zahid Mahmood, Nazeer Muhammad, Nargis Bibi, Tausif Ali, Fractals **25**, 1750025 (2017).
49. B. Mughal, N. Muhammad, M. Sharif, A. Rehman, T. Saba, BMC Cancer A **18**, 778 (2018).
50. Nargis Bibi, A. Kleerekoper, Nazeer Muhammad, Berry Cheetham, SpringerPlus **5**, 931 (2016).